1-1-2010

Analysis of throughput for multilayer infrared meanderline waveplates

Samuel L. Wadsworth
University of Central Florida

Glenn D. Boreman
University of Central Florida

Analysis of throughput for multilayer infrared meanderline waveplates

Samuel L. Wadsworth[1,*] and Glenn D. Boreman[1]

[1]*University of Central Florida, CREOL – The College of Optics and Photonics, 4000 Central Florida Blvd., Orlando, Florida 32816, USA*

**swadswor@creol.ucf.edu*

Abstract: A meanderline wave retarder is a unique type of frequency-selective-surface (FSS) that enables a change in the state of optical polarization. The principles of operation are very similar to a typical crystalline waveplate, such that the artificially structured meanderline array has both 'slow' and 'fast' axes that provide a phase offset between two orthogonal wave components. In this paper, we study the behavior and response of multilayered meanderline quarter-wave retarders designed for operation at 10.6 μm wavelength (28.28 THz). It will be shown that meanderline quarter-wave plates with more than a single layer exhibit improved transmission throughput at infrared frequencies due to impedance matching, similar to a multilayer optical film coating. Numerical data, both from simulations and measurements, are presented to validate this claim.

OCIS codes: (050.6624) Subwavelength structures; (160.3918) Metamaterials; (260.1440) Birefringence; (230.5440) Polarization-selective devices.

References

1. J. S. Tharp, J. M. Lopez-Alonso, J. C. Ginn, C. F. Middleton, B. A. Lail, B. A. Munk, and G. D. Boreman, "Demonstration of a single-layer meanderline phase retarder at infrared," Opt. Lett. **31**(18), 2687–2689 (2006).
2. J. S. Tharp, B. A. Lail, B. A. Munk, and G. D. Boreman, "Design and Demonstration of an Infrared Meanderline Phase Retarder," IEEE Trans. Antenn. Propag. **55**(11), 2983–2988 (2007).
3. J. S. Tharp, J. Alda, and G. D. Boreman, "Off-axis behavior of an infrared meander-line waveplate," Opt. Lett. **32**(19), 2852–2854 (2007).
4. G. P. Nordin, and P. C. Deguzman, "Broadband form birefringent quarter-wave plate for the mid-infrared wavelength region," Opt. Express **5**(8), 163–168 (1999).
5. H. Kikuta, Y. Ohira, and K. Iwata, "Achromatic quarter-wave plates using the dispersion of form birefringence," Appl. Opt. **36**(7), 1566–1572 (1997).
6. D. L. Brundrett, E. N. Glytsis, and T. K. Gaylord, "Subwavelength transmission grating retarders for use at 10.6 μm," Appl. Opt. **35**(31), 6195–6202 (1996).
7. R. B. Boye, S. A. Kemme, J. R. Wendt, A. A. Cruz-Cabrera, G. A. Vawter, C. R. Alford, T. R. Carter, and S. Samora, "Fabrication and measurement of wideband achromatic waveplates for the mid-infrared region using subwavelength features," J. Microlith., Microfab, Microsyst. **5**(4), 043007 (2006).
8. P. C. Deguzman, and G. P. Nordin, "Stacked subwavelength gratings as circular polarization filters," Appl. Opt. **40**(31), 5731–5737 (2001).
9. G. Kang, Q. Tan, X. Wang, and G. Jin, "Achromatic phase retarder applied to MWIR & LWIR dual-band," Opt. Express **18**(2), 1695–1703 (2010).
10. S. A. Kemme, A. A. Cruz-Cabrera, R. R. Boye, T. Carter, S. Samora, C. Alford, J. R. Wendt, G. A. Vawter, and J. L. Smith, "Micropolarizing device for long wavelength infrared polarization imaging," Sandia National Lab., Albuquerque, NM, Sandia Report SAND2006–6889, (2006).
11. A. Lompado, E. A. Sornsin, and R. A. Chipman, "HN22 sheet polarizer, an inexpensive infrared retarder," Appl. Opt. **36**(22), 5396–5402 (1997).
12. R. M. A. Azzam, and C. L. Spinu, "Achromatic angle-insensitive infrared quarter-wave retarder based on total internal reflection at the Si-SiO_2 interface," J. Opt. Soc. Am. A **21**(10), 2019–2022 (2004).
13. M. Iwanaga, "Ultracompact waveplates: approach from metamaterials," Appl. Phys. Lett. **92**(15), 153102 (2008).
14. E. Cojocaru, T. Julea, and F. Nichitiu, "Infrared thin-film totally reflecting quarter-wave retarders," Appl. Opt. **30**(28), 4124–4125 (1991).
15. E. H. Korte, B. Jordanov, D. Kolev, and D. Tsankov, "Total reflection prisms as achromatic IR retarders," Appl. Spectrosc. **42**(8), 1394–1400 (1988).
16. J. Liu, and R. M. A. Azzam, "Infrared quarter-wave reflection retarders designed with high-spatial-frequency dielectric surface-relief gratings on a gold substrate at oblique incidence," Appl. Opt. **35**(28), 5557–5562 (1996).

#127155 - $15.00 USD Received 16 Apr 2010; revised 11 May 2010; accepted 12 May 2010; published 7 Jun 2010

17. V. N. Okorkov, V. Y. Panchenko, B. V. Russkikh, V. N. Seminogov, V. I. Sokolov, and V. P. Yakunin, "Phase retarder for transformation of polarization of high-power infrared laser beams based on resonant excitation of surface electromagnetic waves on metallic diffraction gratings," Opt. Eng. **33**(10), 3145–3155 (1994).
18. E. L. Gieszelmann, S. F. Jacobs, and H. E. Morrow, "Simple quartz birefringent quarter-wave plate for use at 3.39 μm," J. Opt. Soc. Am. A **59**(10), 1381–1383 (1969).
19. R. C. Sharp, D. P. Resler, D. S. Hobbs, and T. A. Dorschner, "Electrically tunable liquid-crystal wave plate in the infrared," Opt. Lett. **15**(1), 87–89 (1990).
20. J. K. Gansel, M. Thiel, M. S. Rill, M. Decker, K. Bade, V. Saile, G. von Freymann, S. Linden, and M. Wegener, "Gold helix photonic metamaterial as broadband circular polarizer," Science **325**(5947), 1513–1515 (2009).
21. P. D. Hale, and G. W. Day, "Stability of birefringent linear retarders (waveplates)," Appl. Opt. **27**(24), 5146–5153 (1988).
22. H. Kikuta, K. Numata, M. Muto, K. Iwata, H. Toyota, K. Moriwaki, T. Yotuya, and H. Sato, "Polarization imaging camera with form birefringent micro-retarder array," in Frontiers in Optics, OSA Technical Digest (CD), (2003).
23. G. P. Nordin, J. T. Meier, P. C. Deguzman, and M. W. Jones, "Micropolarizer array for infrared imaging polarimetry," J. Opt. Soc. Am. A **16**(5), 1168–1174 (1999).
24. C. S. L. Chun, "Microscale waveplates for polarimetric infrared imaging," Proc. SPIE **5074**, 286–297 (2003).
25. M. W. Kudenov, E. L. Dereniak, L. Pezzaniti, and G. R. Gerhart, "2-cam LWIR imaging Stokes polarimeter," Proc. SPIE **6972**, 69720K (2008).
26. M. W. Kudenov, J. L. Pezzaniti, and G. R. Gerhart, "Microbolometer-infrared imaging Stokes polarimeter," Opt. Eng. **48**(6), 063201 (2009).
27. L. Young, L. A. Robinson, and C. A. Hacking, "Meander-line Polarizer," IEEE Trans. Antenn. Propag. **21**(3), 376–378 (1973).
28. R.-S. Chu, and K.-M. Lee, "Analytical method of a multilayered meander-line polarizer plate with normal and oblique plane-wave incidence," IEEE Trans. Antenn. Propag. **35**(6), 652–661 (1987).
29. B. A. Munk, *Finite Antenna Arrays and FSS*, (Wiley, Hoboken, NJ, 2003).
30. C. Terret, J. R. Levrel, and K. Mahdjoubi, "Susceptance computation of a meander-line polarizer layer," IEEE Trans. Antenn. Propag. **32**(9), 1007–1011 (1984).
31. A. K. Bhattacharyya, and T. J. Chwalek, "Analysis of multilayer meanderline polarizer," Int. J. Microwave Millimeter-Wave Comput.-Aided Eng. **7**(6), 442–454 (1998).
32. Z. Knittl, *Optics of thin films; an optical multilayer theory*, (Wiley, New York, NY, 1976).
33. H. A. Macleod, *Thin-film optical filters*, (American Elsevier, New York, NY, 1969).
34. P. A. Rizzi, *Microwave Engineering: Passive Circuits*, (Prentice-Hall, Upper Saddle River, NJ, 1988).
35. K. K. Chan, T. W. Ang, T. H. Chao, and T. S. Yeo, "Accurate analysis of meanderline polarizers with finite thicknesses using mode matching," IEEE Trans. Antenn. Propag. **56**(11), 3580–3585 (2008).
36. E. D. Palik, *Handbook of optical constants of solids, vol. III.*, (Academic, San Diego, CA, 1997).
37. P. Garrou, "Polymer dielectrics for multichip module packaging," Proc. IEEE **80**(12), 1942–1954 (1992).
38. W. R. Folks, J. C. Ginn, D. J. Shelton, J. S. Tharp, and G. D. Boreman, "Spectroscopic ellipsometry of materials for infrared micro-device fabrication," Phys. Status Solidi **5**(5), 1113–1116 (2008) (c).
39. J. S. Tharp, D. J. Shelton, S. L. Wadsworth, and G. D. Boreman, "Electron-beam lithography of multiple-layer submicrometer periodic arrays on a barium fluoride substrate," J. Vac. Sci. Technol. B **26**(5), 1821–1823 (2008).
40. D. Goldstein, *Polarized Light 2nd Ed.*, (Marcel Dekker, New York, NY, 2003).
41. J. E. Raynolds, B. A. Munk, J. B. Pryor, and R. J. Marhefka, "Ohmic loss in frequency-selective surfaces," J. Appl. Phys. **93**(9), 5346–5358 (2003).
42. L. Mandel, and E. Wolf, *Optical Coherence and Quantum Optics*, (Cambridge, New York, NY, 1995).
43. D. F. Bezuidenhout, K. D. Clarke, and R. Pretorius, "The optical properties of YF_3 films," Thin Solid Films **155**(1), 17–30 (1987).
44. J. Y. Robic, B. Rolland, J. C. Deutsch, and P. Gallais, "Ion-assisted deposition of yttrium fluoride as a substitute for thorium fluoride: Application to infrared anti-reflection coating on germanium," Proc. SPIE **2253**, 552–558 (1994).
45. V. K. Arora, "Quantum size effect in thin-wire transport," Phys. Rev. B **23**(10), 5611–5612 (1981).

1. Introduction

The generation of circularly polarized light for infrared (IR) frequencies has been subject to a host of birefringent materials and mechanisms [1–20] that aim to produce 90° phase shift between orthogonal electromagnetic field components. Conventional single-crystal waveplates are most commonly used for single-frequency operation at normal incidence, since the birefringence is limited by the dispersion and thickness of the material, which is also sensitive to angular divergence [21]. Certain birefringent crystals, such as quartz [18], are not appropriate for use at longer IR wavelengths due to inherent absorption resonances beyond 5 μm. Other methods aim to tailor the differential phase shift upon reflection, either from thin film layers [12,14], prisms [15], or subwavelength gratings [16,17]. Although such techniques have been proven to be functional over multiple IR wavelengths and angles, the actual mechanisms require the optical system to be specifically designed for reflection from the

#127155 - $15.00 USD Received 16 Apr 2010; revised 11 May 2010; accepted 12 May 2010; published 7 Jun 2010

devices themselves, which is not advantageous for integration into a preexisting optical system. Therefore, the interest in imaging polarimetry at IR frequencies [22–26] in both mid-wave (MWIR, 3–5 μm) and long-wave (LWIR, 8–12 μm) bands has prompted investigation into artificial birefringent materials [1–10,13,20] that are able to perform across the entire wavelength band of interest, and have the capability of being integrated onto the focal plane array (FPA) of an IR imaging system. Such investigations have been conducted with form-birefringent structures [4–10], which are corrugated subwavelength gratings etched into high-index material. The contrast between the optically-dense substrate material and the filling medium, along with a polarization-dependent effective refractive index, provides a suitable birefringence for achromatic quarter-wave plate (QWP) operation throughout the MWIR or LWIR bands. These studies have also shown that form-birefringent structures respond well, even in angular diverging radiation [5,7,9,10], which facilitates integration of the form-birefringent QWP's into IR polarimeters. However, since the recent exploration of meanderline wave retarders in the IR [1–3], there has not been any analysis of multilayered meanderline QWP's for potential polarimetry applications. The biggest obstacle that has to be addressed with regard to meanderline retarders for IR imaging and polarimetry is their power transmission performance, especially since form-birefringent retarders exhibit over 70% throughput [5–10]. Thus, it is our goal to design and construct 1-layer, 2-layer, and 3-layer meanderline polarizers for QWP operation at 10.6 μm, and to investigate their transmission throughput potential.

2. Transmission line circuit model for multilayer meanderline polarizers

A common approach for describing the behavior of multilayer meanderline polarizers has been to represent the artificially structured surface as a lumped impedance circuit discontinuity. This has been the case historically for analyzing multilayer meanderline retarders at THz or microwave frequencies [27–31], and is a viable approach for modeling the behavior in the IR. As Fig. 1 illustrates, the equivalent circuit model of meanderline FSS elements can be thought of as two separate transmission line circuits that correspond to TE and TM radiation. The TM mode induces a current to flow along the metallic elements, which corresponds to inductive impedance. Likewise, the TE polarization encounters capacitive impedance due to the capacitive-type field mode in the apertures adjacent to the metallic elements.

#127155 - $15.00 USD Received 16 Apr 2010; revised 11 May 2010; accepted 12 May 2010; published 7 Jun 2010

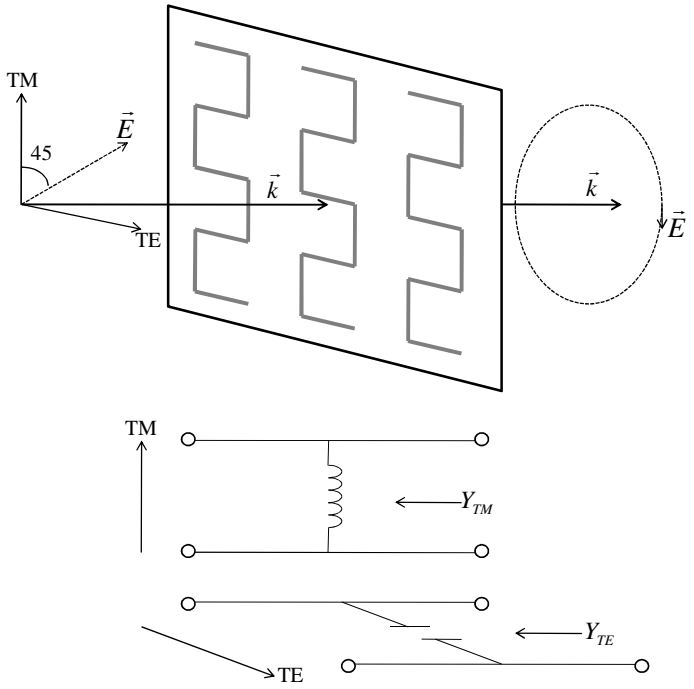

Fig. 1. Meanderline polarizer array for conversion of linear to circular polarization. Note that the incident polarization state has to be linear and rotated 45° about the meanderline axis so that equal components of the incident field pass through the TE and TM polarization modes.

The equivalent transmission line circuit model can also be thought of as a multilayered optical system. Since the meanderline element thickness is much smaller than the wavelength, it can be modeled as an infinitesimally thin sheet that has equivalent surface impedance, which can therefore be combined with the surrounding media as an effective surface-impedance discontinuity. From optical multilayer theory [32,33], we know that the reflection from a surface interface can be written in terms of the surrounding material impedance. Therefore, transmission through a multilayered meanderline structure can be modeled as a thin-film optical coating with the appropriate equivalent surface impedance at the meanderline surface discontinuity. Thus, what follows is a hybridization of both circuit transmission line [27–31] and optical multilayer theory [32,33] for describing the transmission of IR radiation through multilayered meanderline polarizers. This description is used to formulate our multilayer designs in obtaining optimum transmission throughput.

Consider a generic multilayer structure comprised of multiple meanderline layers that are separated by interstitial layers of dielectric media. Assume that the first meanderline layer is facing towards free space, and that each corresponding dielectric layer that proceeds a given meanderline layer can be combined into a sort of replicated unit cell. Referring to Fig. 2, each effective unit cell can be described in terms of the surrounding material impedance, the propagation through the dielectric medium, and the equivalent surface impedance discontinuity that represents the FSS layer. Mathematically, this can be written as

$$Y_k = n_k \cdot Y_o = 1/Z_k, \tag{1a}$$

$$\beta_k = 2\pi \cdot n_k / \lambda_0, \tag{1b}$$

where Y_k is the material admittance for the dielectric layer of the k^{th} unit cell, β_k is the associated propagation constant, n_k is the complex index of refraction, Y_0 is the characteristic admittance of free space (1/377 Siemens), and λ_0 is the free space wavelength. The equivalent

#127155 - $15.00 USD Received 16 Apr 2010; revised 11 May 2010; accepted 12 May 2010; published 7 Jun 2010

surface admittance of the meanderline layer is given by Y_{mk}, and t_k is the thickness of the dielectric layer. At this point, it should be noted that the equivalent impedance of the materials and surface layers can be written in terms of admittance values. This will be done throughout the rest of this paper.

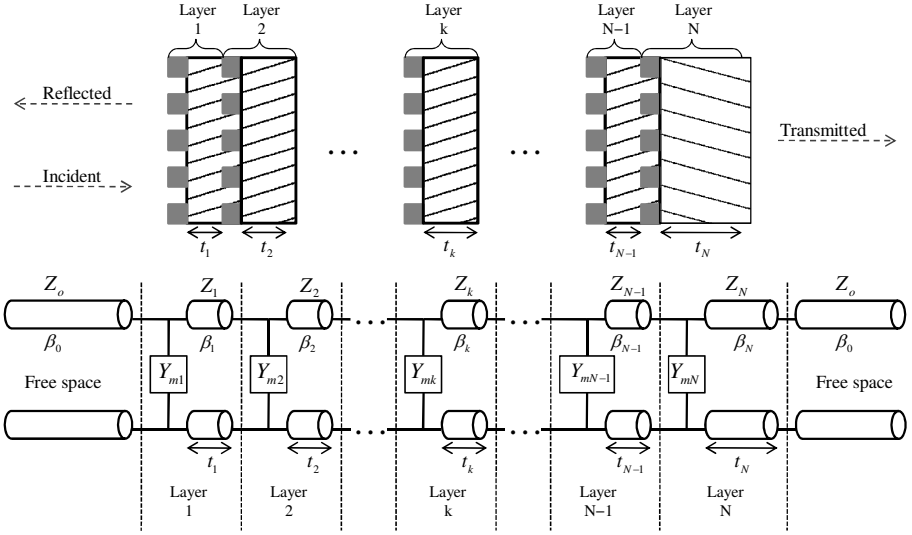

Fig. 2. Multilayer meanderline polarizer configuration with corresponding circuit model. Note that the k^{th} unit cell (meanderline surface with dielectric layer) is the repeating element in the multilayer stack-up.

To determine the transmission coefficient from a multilayer structure, each individual meanderline-dielectric layer combination can be written in terms of a wave transmission matrix [28,30,32,34] that describes the surface admittance discontinuity at the meanderline layer and the propagation through the dielectric layer. For the k^{th} unit cell of the multilayered structure,

$$T_k = T_B \cdot T_A, \tag{2a}$$

$$T_A = \frac{1}{2} \cdot \begin{bmatrix} \left(1+\frac{Y_{k-1}}{Y_k}\right)-\frac{Y_{mk}}{Y_k} & \left(1-\frac{Y_{k-1}}{Y_k}\right)-\frac{Y_{mk}}{Y_k} \\ \left(1-\frac{Y_{k-1}}{Y_k}\right)+\frac{Y_{mk}}{Y_k} & \left(1+\frac{Y_{k-1}}{Y_k}\right)+\frac{Y_{mk}}{Y_k} \end{bmatrix}, \tag{2b}$$

$$T_B = \begin{bmatrix} \exp\left(i \cdot \beta_k \cdot t_k\right) & 0 \\ 0 & \exp\left(-i \cdot \beta_k \cdot t_k\right) \end{bmatrix}. \tag{2c}$$

In the preceding equations, Y_{k-1} is the material admittance of the dielectric layer for the $(k-1)^{th}$ unit cell. The individual matrices T_A and T_B represent the surface admittance discontinuity and the propagation through the dielectric layer, respectively. For a multilayer system with N respective unit cells, the total system matrix would be

$$\overline{T} = \begin{bmatrix} \overline{T}_{11} & \overline{T}_{12} \\ \overline{T}_{21} & \overline{T}_{22} \end{bmatrix} = T_N \cdot T_{N-1} \cdots\cdots T_k \cdots\cdots T_2 \cdot T_1. \tag{3}$$

As an added correction, if the last unit cell in the system has a finite dielectric thickness whose back side faces towards free space, we can say that

#127155 - $15.00 USD Received 16 Apr 2010; revised 11 May 2010; accepted 12 May 2010; published 7 Jun 2010

$$T_N = T_C \cdot T_B \cdot T_A, \tag{4}$$

where T_A and T_B are the same as Eqs. (2)b) and (2c) for $k = N$, and T_C is given by

$$T_C = \frac{1}{2} \cdot \begin{bmatrix} \left(1 + \frac{Y_N}{Y_0}\right) & \left(1 - \frac{Y_N}{Y_0}\right) \\ \left(1 - \frac{Y_N}{Y_0}\right) & \left(1 + \frac{Y_N}{Y_0}\right) \end{bmatrix}. \tag{5}$$

The individual matrix elements in Eq. (3) can then be utilized to obtain the amplitude reflection and transmission coefficients:

$$\Gamma = \frac{-\bar{T}_{12}}{\bar{T}_{11}}, \tag{6a}$$

$$\tau = \frac{1}{\bar{T}_{11}} \cdot \det\left(\bar{T}\right). \tag{6b}$$

In Eq. (6)b), $\det(\bar{T})$ is the determinant of the system matrix, and is given by the expression Y_0/Y_f, where Y_f represents the admittance of the final optical layer. In most cases, Y_f is free space, so the value of $\det(\bar{T})$ results in unity. Likewise, the power reflection and transmission coefficients are the following:

$$R = \left|\Gamma\right|^2, \tag{7a}$$

$$T = \left|\tau\right|^2 \cdot \mathrm{Re}\left(n_f\right), \tag{7b}$$

where n_f is the complex index of refraction of the last medium through which the optical wave propagates. Since the multilayered structure is surrounded by free space, n_f is just the refractive index of air.

3. Parameter extraction of meanderline admittances and calculation of the power transmission coefficient

Considering that the power transmission coefficient is the desired parameter from the above matrix formulation, the admittance of the individual meanderline layers has to be known in order to effectively calculate the power throughput. However, for each single meanderline layer, there are two separate effective admittances that have to be determined, since the geometry of the structure indicates anisotropic behavior for the respective incident TE and TM polarizations [1–3,27–31,35]. Because the meanderline polarizer exhibits different admittances for the orthogonal TE and TM polarizations, the transmission coefficients have to be calculated separately for each case. Before this can be done, however, the meanderline admittances must be extracted for the TE and TM modes. The admittances have to be rigorously solved by computational means, which include periodic moment methods and mode matching techniques [1–3,28,30,31,35]. We will make use of a commercial finite-element method full wave solver (Ansoft HFSS) to extract the effective impedance of a single meanderline surface discontinuity within the multilayer stack.

To do this, we select the meanderline layer of interest, say layer j, in the multilayer structure. The other meanderline layers in the stack are temporarily removed from the model so that the j^{th} layer is the only one remaining. With reference to Eqs. (2)b) and (2c), Y_{mk} is non-zero when $k = j$. Otherwise, $Y_{mk} = 0$ for all $k \neq j$. The equivalent model in the finite-element solver reflects this condition. Then, the remaining structure is solved within the HFSS program and the complex amplitude reflection coefficient in Eq. (6)a) is acquired for both TE and TM polarizations. Since there is only one meanderline admittance to solve for with regard

#127155 - $15.00 USD Received 16 Apr 2010; revised 11 May 2010; accepted 12 May 2010; published 7 Jun 2010

to each polarization state, Eq. (6)a) can then be used to determine Y_{mk}. For instance, a single-layer meanderline polarizer (N = 1) will have the following complex amplitude reflection coefficient, which is determined from the system matrix parameters of Eq. (3) and solved directly within HFSS:

$$\Gamma = \frac{-\left(e^{-i\cdot\beta_1\cdot t_1}\cdot\left(\frac{Y_1}{Y_0}-1\right)\cdot\left(\frac{Y_0}{Y_1}+\frac{Y_{m1}}{Y_1}+1\right)+e^{i\cdot\beta_1\cdot t_1}\cdot\left(\frac{Y_1}{Y_0}+1\right)\cdot\left(\frac{Y_0}{Y_1}+\frac{Y_{m1}}{Y_1}-1\right)\right)}{e^{-i\cdot\beta_1\cdot t_1}\cdot\left(\frac{Y_1}{Y_0}-1\right)\cdot\left(-\frac{Y_0}{Y_1}+\frac{Y_{m1}}{Y_1}+1\right)-e^{i\cdot\beta_1\cdot t_1}\cdot\left(\frac{Y_1}{Y_0}+1\right)\cdot\left(\frac{Y_0}{Y_1}-\frac{Y_{m1}}{Y_1}+1\right)}. \quad (8)$$

Solving for the meanderline admittance Y_{m1} will then yield the following:

$$Y_{m1} = \frac{2Y_0Y_1\Gamma\cos(\beta_1 t_1)+i\cdot\sin(\beta_1 t_1)\cdot\left((1+\Gamma)Y_1^2+(-1+\Gamma)Y_0^2\right)}{(1+\Gamma)\left(Y_1\cos(\beta_1 t_1)+i\cdot Y_0\sin(\beta_1 t_1)\right)}. \quad (9)$$

The solutions for the admittances of a 2-layer or 3-layer meanderline polarizer structure will be fairly similar to Eq. (9), but with more propagation constants and reflection terms to account for the inclusion of additional layers. Note that the meanderline admittance in Eq. (9) depends upon which of the two reflection coefficients are inserted into the formula. For instance, if the complex TE reflection coefficient is used, then the resulting admittance will correspond to the TE mode of the meanderline polarizer layer. Likewise, the admittance for the TM mode will be obtained by using the complex TM amplitude reflection coefficient.

After solving for all N meanderline admittances by using the aforementioned method, the admittance values can be substituted back into the expression for each layer in Eq. (2)b). Ultimately, the system matrix of Eq. (3) and the power transmission coefficient of Eq. (7)b) can be calculated from the N-layer matrix equation for both TE and TM polarizations. If desired, the power transmission coefficients can then be averaged to obtain the total power transmission:

$$T_{total} = \frac{1}{2}\cdot\left(T_{TE}+T_{TM}\right). \quad (10)$$

The transmitted phase shift δ between the two orthogonal polarizations can be deduced from the complex amplitude transmission coefficient in Eq. (6)b):

$$\delta = \left|\arctan\left(\frac{\mathrm{Im}(\tau_{TE})}{\mathrm{Re}(\tau_{TE})}\right)-\arctan\left(\frac{\mathrm{Im}(\tau_{TM})}{\mathrm{Re}(\tau_{TM})}\right)\right|. \quad (11)$$

This approach solves each layer one at a time and combines the solved admittances into the wave transmittance matrix method (TMM). Therefore, each meanderline layer is effectively acting on its own without any coupling between adjacent layers. This segmented approach is consistent with other such methods that solve for the meanderline admittances separately on a layer-by-layer basis [28,30,31,35]. Thus, comparisons between this approach and solving the entire structure within HFSS are quite useful, especially for determining any differences in the numerical results that are due to mutual admittance coupling and other full wave effects. Furthermore, the TMM will be used to compute the interlayer dielectric thickness that results in an admittance-matched multilayer meanderline structure, which indicates that a maximum transmission throughput and corresponding reflection minimum has been obtained. Results from both of these numerical techniques will be compared to the experimental transmission data from 1-layer, 2-layer, and 3-layer meanderline polarizers.

It should be mentioned that although the TMM approach was performed for a single wavelength at normal incidence, it can be done over multiple frequencies at various non-zero angles of incidence with only a slight modification to the formulas in the previous section [28].

#127155 - $15.00 USD Received 16 Apr 2010; revised 11 May 2010; accepted 12 May 2010; published 7 Jun 2010

4. Design of multilayer meanderline retarders for 10.6 μm

Meanderline retarders have been successfully designed and fabricated for many years in the RF band [27–31,35]. In order to effectively scale the polarimetric behavior of these devices to the LWIR, the physical dimensions need to be reduced to sub-micron linewidths. Appropriate materials also have to be chosen so that the power transmission remains as high as possible. Therefore, the selection of fabrication materials was implemented as the first step of the design phase for each meanderline polarizer. The ideal materials for these multilayer devices consist of the following specifications: high conductivity metals, relatively low refractive index dielectrics, low absorption loss, and compatibility with existing fabrication processes. The materials that were chosen to meet these requirements include a highly-transmissive Barium Fluoride (BaF_2) substrate, metallic Aluminum (Al) for the meanderline circuit elements, and Benzocyclobutene (BCB) for the dielectric standoff layers. BaF_2 has one of the highest transmission throughputs in the IR, and is often used as a window for IR and visible applications [36]. Al was used because of its relatively high DC conductivity and low absorption loss in the LWIR. Although there are some lower-loss choices for the dielectric standoff layer material, BCB was selected due to its ease of use and compatibility with multilayer device fabrication [37]. The optical properties of each material were measured via IR ellipsometry [38] and are included in Table 1. The DC conductivity of Al is determined by

$$\sigma_{DC} = 2nk\omega\varepsilon_0, \tag{12}$$

where n and k are the optical constants of Al, ω is the angular frequency, and ε_0 is equal to the permittivity of free space ($8.8542 \cdot 10^{-12}$ F/m).

Table 1. Optical constants of fabrication materials at 10.6 μm

Material	n	k
BCB	1.55913	0.042235
BaF_2	1.39262	$1.6982 \cdot 10^{-5}$
Al	23.9207	46.1554

Once the materials were selected, corresponding models for the 1-layer, 2-layer, and 3-layer polarizers were constructed in the full-wave electromagnetic solver program. The linewidths, metal thickness, and array spacings were iteratively adjusted for each meanderline layer until a 90° phase shift was obtained at 10.6 μm under normal incidence. For the 2-layer and 3-layer devices, the thickness of each BCB standoff layer was initially defined as $\lambda_0/4n$, where n is the refractive index of BCB. After refinement of the array dimensions was complete, the effective meanderline admittances were extracted using the method outlined in the previous section. The complex amplitude reflection coefficients for both TE and TM polarizations were then calculated over a wide range of thicknesses for the dielectric standoff layer. This procedure was done twice for the 3-layer polarizer, since it has two separate standoff layers that can vary in thickness. Ultimately, the desired thicknesses of the standoff layers were found when the absolute value of the complex reflection coefficient reached an average minimum between the TE and TM polarizations. The optimum thicknesses were inserted into the full-wave solver and the meanderline array dimensions were slightly adjusted to give the optimal phase shift and power transmission response. The resulting dimensions for each of the three multilayer meanderline polarizers are given in Table 2. Figure 3 illustrates the array parameters for a single unit cell and the corresponding multilayer configuration for each meanderline polarizer structure.

#127155 - $15.00 USD Received 16 Apr 2010; revised 11 May 2010; accepted 12 May 2010; published 7 Jun 2010

Table 2. Array dimensions for the multilayer QWP's (in μm)[a]

	lw1	lw2	lw3	DX	DY	pw	ph	t_1	t_2
1-layer	0.45	0.8	0.45	2	1.7	1	1.1		
2-layer	0.4	0.4	0.4	2	2.7	1	1.1	1.5	
3-layer	0.2	0.2	0.2	2	2.75	1	1.1	1.13	1.3

[a]Note that, for the 2-layer and 3-layer polarizers, the array dimensions are the same on each layer. Also, the thickness of metal was set at 60 nm for all layers on each device.

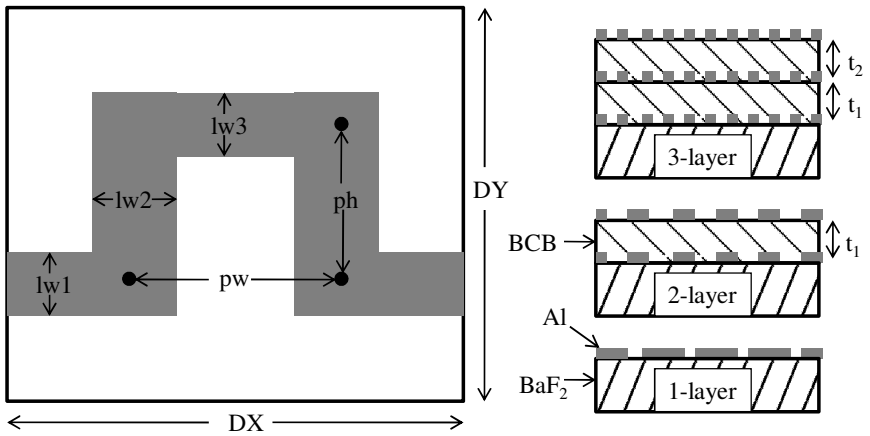

Fig. 3. Unit cell and multilayer geometries for a meanderline polarizer. The lengths t_1 and t_2 are thicknesses of the BCB dielectric layers.

5. Fabrication and testing

Fabrication of the sub-micron meanderline array features was carried out on a Leica EBPG 5000 + electron beam lithography system. This system has a lower resolution limit of about 20 nm, which allows for high-quality reproduction of metallic patterns. In order to successfully fabricate the patterns onto BaF_2 substrates and BCB dielectric layers, special processing techniques had to be used so that excess charging of the substrate and electron beam resist did not occur. The process that was implemented follows directly from [39], with the only change being the electron beam dosage that was used to write the various meanderline array geometries listed in Table 2. A scanning electron micrograph (SEM) of each structure can be found on Fig. 4. It should be noted that the images corresponding to the 2-layer and 3-layer polarizers were taken on a single meanderline layer of the multilayered structure.

#127155 - $15.00 USD Received 16 Apr 2010; revised 11 May 2010; accepted 12 May 2010; published 7 Jun 2010

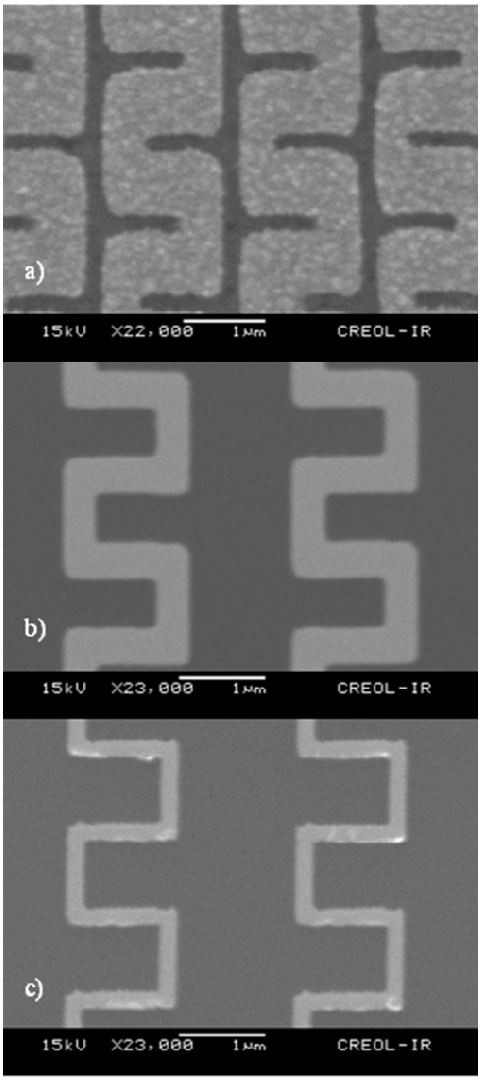

Fig. 4. SEM micrograph of a single meanderline layer of each multilayer structure. The individual images marked a), b), and c) represent the metalized patterns for the 1-layer, 2-layer, and 3-layer devices, respectively.

Once each device was completed, characterization was done solely on the Infrared Variable Angle Spectroscopic Ellipsometer (IR-VASE) from J.A. Woollam. The IR-VASE apparatus is normally used to measure the thickness and optical properties of thin films in reflection mode from 2 μm to 30 μm [38]. However, the system can be configured for transmission mode at normal incidence to directly measure the phase shift and axial ratio of the optical beam that passes through a multilayer meanderline polarizer structure. The phase shift was obtained by initiating a standard spectroscopic scan, which extracts parameters ψ and δ from the polarimetric measurements. The parameter δ is the phase shift between the transmitted TE and TM polarization modes, where as ψ is the auxiliary angle of the polarization ellipse. These quantities were utilized to directly compute the axial ratio, which is defined as the ratio between the major and minor axes of the polarization ellipse [1–3,40]:

$$AR = 1 \Big/ \left(\tan\left[\frac{1}{2} \arcsin\left\{ \sin\left(2 \cdot \psi\right) \cdot \sin\left(\delta\right) \right\} \right] \right). \tag{13}$$

#127155 - $15.00 USD Received 16 Apr 2010; revised 11 May 2010; accepted 12 May 2010; published 7 Jun 2010

The same IR-VASE system was also used to perform a power transmission scan for each multilayer meanderline retarder. This measurement collects the power transmission coefficients listed in Eq. (10) for both TE and TM polarization states. The pre-set coordinate system on the IR ellipsometer, which is shown on Fig. 5, facilitated alignment and subsequent measurements so that each orthogonal state of polarization directly corresponded to the TE and TM modes of the meanderline polarizer under test. Since the power transmission and spectroscopic ellipsometry measurements are completely automated, the meanderline polarizer has to be aligned to this coordinate system so that accurate readings can be acquired for the polarimetric quantities ψ, δ and the power transmission coefficients.

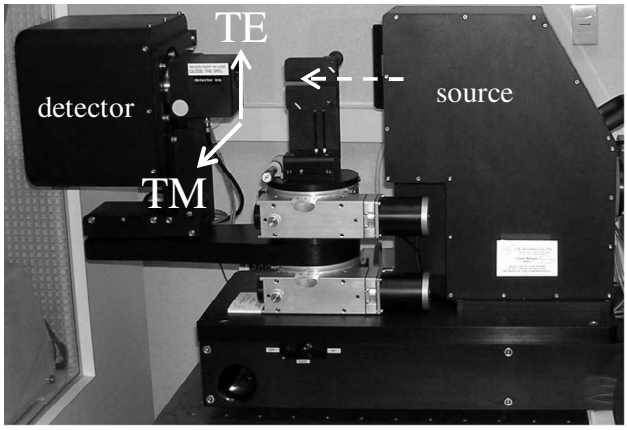

Fig. 5. Pre-set coordinate system on IR ellipsometer. The dashed arrow indicates the direction of beam propagation from the source. The IR-VASE has a built-in linear polarizer that automatically selects the TE or TM mode for analysis.

6. Results and discussion

In order to gauge the performance of the multilayered meanderline retarders, the axial ratio (Eq. (13)), the differential phase shift (Eq. (11)), and the total power transmission (Eq. (10)) will be presented. Table 3 summarizes these results for both the numerical and experimental data at 10.6 μm. Recall that the design goals for the phase shift and axial ratio of each multilayered structure were 90° and 1, respectively.

#127155 - $15.00 USD Received 16 Apr 2010; revised 11 May 2010; accepted 12 May 2010; published 7 Jun 2010

Table 3. Experimental and numerical results for multi-layered meanderline QWP's operating at 10.6 μm.

	δ	AR	T_{total}
1-layer QWP			
Experiment	77.79° ± 0.678°	1.972 ± 0.0103	36.84% ± 0.367%
Ansoft HFSS	81.02°	1.604	39.43%
TMM	96.95°	1.998	39.41%
2-layer QWP			
Experiment	86.51° ± 0.909°	1.206 ± 0.006	65.81% ± 0.652%
Ansoft HFSS	89.37°	1.226	67.89%
TMM	92.65°	1.375	68.50%
3-layer QWP			
Experiment	83.38° ± 0.753°	1.253 ± 0.008	58.09% ± 0.783%
Ansoft HFSS	82.18°	1.259	59.41%
TMM	82.25°	1.372	60.53%

Most of the numerical results, from the HFSS model and from the wave TMM approach, agree very well with the corresponding experimental data. However, the axial ratio of the single-layer meanderline polarizer predicted by HFSS shows some discrepancy, as compared to the measured value. This could be attributed to structural non-idealities that occurred during fabrication, such as over-exposure of the critical linewidths, or surface roughness upon the metallic Al meanderline elements. Additionally, the predicted phase shift given by the TMM model deviates by about 15% from the expected measured value for the single-layer meanderline retarder. Recall that the TMM algorithm uses the complex amplitude reflection coefficient to solve for the equivalent surface admittance of a given meanderline surface discontinuity. When calculating the equivalent parameters for a meanderline layer with a high proportion of metal, the reflection coefficient only registers the properties of a highly-reflective surface. Thus, certain information from a highly-reflective meanderline surface does not get imparted to the reflection coefficient, such as the absorption loss that occurs upon transmission through the meanderline layer. Therefore, the predicted phase shift from the TMM model for a single layer meanderline QWP does not account for the ohmic losses [41] from within the metallic elements, which duly affect the polarimetric quantities that are predicted by full-wave HFSS simulations. However, for meanderline structures with more than a single layer, the TMM model increases in accuracy, since the magnitude of absorption loss decreases along with the metal fill factor for a single layer embedded in a multilayer stack.

With regard to the fill factor of the meanderline layers, it is interesting to note that, in order to obtain QWP behavior for all three multilayered devices, there are certain constraints on the circuit-element dimensions that were set during the design phase, which not only affect the polarimetric behavior, but also the transmission response. One can see that, for an N-layered meanderline QWP, the accumulated phase shift can be distributed between each successive layer, such that each layer contributes $\pi/2N$ phase shift. Accordingly, the dimensions of the meanderline elements required to produce such distributed phase shifts can be subsequently relaxed as the number of layers N increases. By this, we mean that the circuit linewidths are able to be reduced in dimension, which likewise reduces the magnitude of the inductive and capacitive admittance phase offsets [28–31]. Referring to the SEM images of each multilayer structure on Fig. 4, we see that this is exactly the case, as the increase in layer count allows for the respective circuit linewidths on each layer to decrease in order to maintain QWP behavior. However, with the increase in number of layers, one would initially presume that the accumulative absorption loss would also increase. From a pure fill-factor

#127155 - $15.00 USD Received 16 Apr 2010; revised 11 May 2010; accepted 12 May 2010; published 7 Jun 2010

standpoint, we find that this is not true, since the *total* percentage of metal in a multilayered QWP stack actually *decreases* with increasing number of meanderline layers. Figure 6 shows the fill-factor-based power transmission for a single layer and the corresponding multilayer structure, where the transmittance is simply given by

$$T = \left(1 - FF\right)^N , \tag{14}$$

where N is the number of layers, and FF is the metallic fill-factor percentage for a given unit cell design of a multilayer meanderline polarizer, whose dimensions are given on Table 2. Not only do we observe greater transmittance for more layers of a meanderline QWP, but we also see that the above formula, simple as it may be, is not a valid criterion for predicting the upper limit of power transmission throughput for a multilayered device. Besides not accounting for full-wave phenomenon, such as edge diffraction and surface wave scattering, the phase information that accumulates between the layers is not accounted for. In our previous treatment of the multilayer problem by means of TMM, the spacing, and thus, the phase separation between the meanderline layers plays an important role in determining the magnitude of the transmission coefficient. Therefore, the neglect of multilayer interference inhibits Eq. (14) from making an accurate prediction for the power transmission throughput, since spatial coherence is preserved at length scales that are shorter than the operating wavelength [42]. However, if we were to separate each individual meanderline layer by hundreds of waves, then with the decrease in coherence, we might see more agreement with the predictions from this simple approximation.

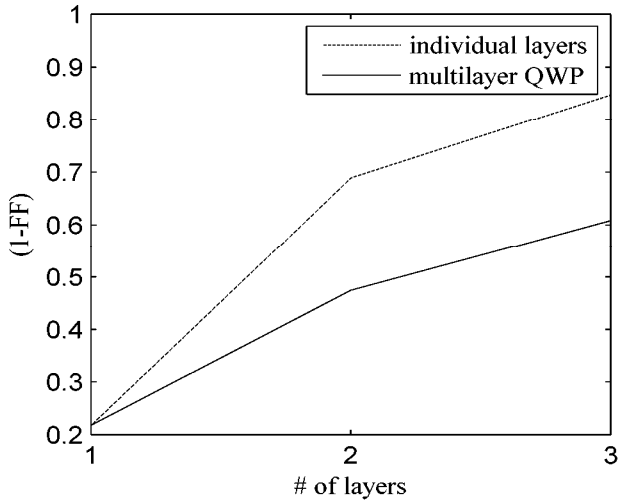

Fig. 6. Fill-factor based transmission through a single layer, and a multilayer structure designed to give QWP behavior.

Selecting the best multilayer polarizer from those listed on Table 3, it is seen that the 2-layer structure exhibits both the best transmission and polarimetric characteristics of the three devices that were fabricated. This result might come as a surprise, since the 3-layer QWP has an additional meanderline layer which can match the admittance of the other layers at 10.6 μm, thereby resulting in increased potential power transmission. The limitation in this instance is the spin-on dielectric BCB that was used for the standoff layers. BCB has significant absorption effects in the LWIR band, which are seen in Fig. 7. Thus, even though we would expect an increase in transmission throughput for the 3-layer structure, propagation through more than 2 μm of BCB mitigates any gains because of the accumulated absorption loss.

#127155 - $15.00 USD Received 16 Apr 2010; revised 11 May 2010; accepted 12 May 2010; published 7 Jun 2010

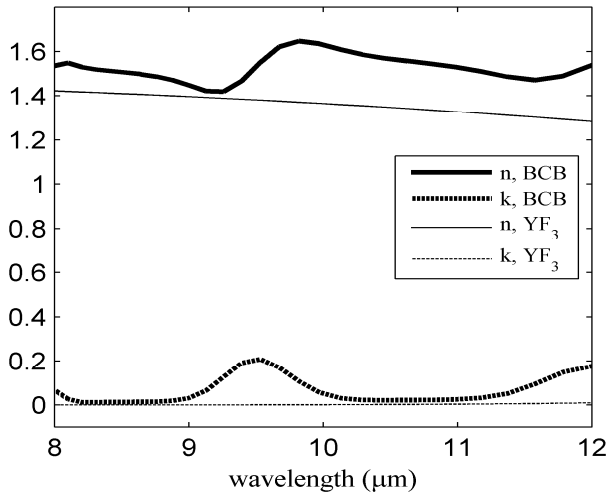

Fig. 7. Optical constants of BCB and YF_3 thin films in the LWIR.

Since the 2-layer structure has 1.5 μm of deposited BCB, it wins outright simply because of decreased attenuation of optical transmittance. Alternate solutions for a suitable standoff layer have been considered, one possible choice being Yttrium Fluoride (YF_3). YF_3 is a ceramic material and fluoride compound, and is usually deposited via sputtering or evaporation [43,44]. Its optical properties were measured via IR ellipsometry and are seen in Fig. 7. This particular material was not included in the current study due to the fact that it is difficult to deposit and process, and especially since it is known to contaminate evaporation chambers that would otherwise be used for multiple materials and processes. However, it exhibits very low loss in the LWIR band, so it would constitute the ideal material candidate for multilayer polarizers, or general highly-transmissive metamaterials for the infrared. Figure 8 shows the simulated power transmission and differential phase shift response for 2-layer and 3-layer meanderline QWP's that were designed for a center wavelength of 10.6 μm. The YF_3 dielectric material was included in the standoff layers.

#127155 - $15.00 USD Received 16 Apr 2010; revised 11 May 2010; accepted 12 May 2010; published 7 Jun 2010

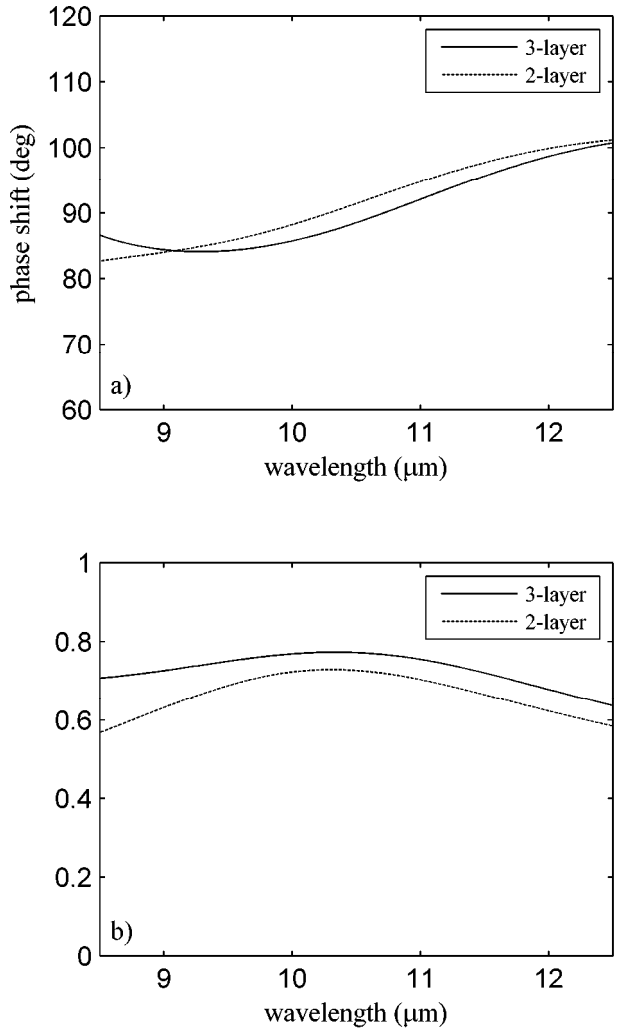

Fig. 8. Simulated a) phase shift and b) power transmission response for 2-layer and 3-layer meanderline QWP's with YF_3 standoff layers.

Note that the 3-layer polarizer exhibits an increase in peak power transmission over multiple wavelengths, since each meanderline layer can match the effective admittance of the other layers at more frequency points, similar to a multilayer optical coating [32,33]. Similar gains in the power transmission response would also be expected for structures with even more meanderline layers. Even so, there may be a practical limit to this extrapolation, since the reduction of circuit linewidths for additional layers might conflict with fabrication tolerances, or might even introduce non-ideal skin depth or quantum related effects for extremely thin metal wires [45]. Nonetheless, the inclusion of additional meanderline layers provides a design utility that assists in increasing the broadband spectral transmission throughput of a multilayer meanderline quarter-wave retarder.

7. Conclusions and future work

We have shown that equivalent transmission line circuit models of multilayer meanderline polarizers designed for 10.6 μm are quite accurate in terms of predicting the polarimetric and transmission response. The transmission line TMM approach is also useful for admittance-matching multiple layers of stratified meanderline retarders for obtaining optimum

#127155 - $15.00 USD Received 16 Apr 2010; revised 11 May 2010; accepted 12 May 2010; published 7 Jun 2010

transmission throughput. By using this method along with full-wave numerical simulations and comparisons with measured data, we have shown that the peak power transmission of a multilayer meanderline QWP depends upon four key points; the design and dimensions of a meanderline unit cell, the number of meanderline layers in a given stack, the thickness of the interlayer dielectric, and the type of dielectric material that serves as the standoff layer between adjacent meanderline sheets. The spin-on dielectric film of BCB was primarily used to facilitate fabrication of the multilayer structures, since a validated process for BCB already existed [38]. However, given the appropriate procedures and methods, a similar process could also be developed so that YF_3 can be inserted into the fabrication routine for multilayer waveplates. Therefore, with the right combination of layers and materials, one could design and fabricate a multilayer meanderline QWP for the LWIR that would be suitable for broadband imaging and polarimetry applications.

Acknowledgements

This work was supported in part by DRS, Optronics division, and by the Florida High-Tech Corridor Council.

#127155 - $15.00 USD Received 16 Apr 2010; revised 11 May 2010; accepted 12 May 2010; published 7 Jun 2010